Flip-Chip-Based Fast Inductive Parity Readout of a Planar Superconducting Island

M. Hinderling,[1] S.C. ten Kate,[1] D.Z. Haxell,[1] M. Coraiola,[1] S. Paredes,[1] E. Cheah,[2] F. Krizek,[1,2,†] R. Schott,[2] W. Wegscheider,[2] D. Sabonis,[1] and F. Nichele[1,*]

[1] IBM Research Europe—Zurich, Säumerstrasse 4, Rüschlikon 8803, Switzerland
[2] Solid State Physics Laboratory, ETH Zurich, Otto-Stern-Weg 1, Zürich 8093, Switzerland

(Received 14 October 2023; revised 3 June 2024; accepted 8 July 2024; published 20 August 2024)

The properties of superconducting devices depend sensitively on the parity (even or odd) of the quasiparticles that they contain. Encoding quantum information in the parity degree of freedom is central in several emerging solid-state qubit architectures, including in hybrid superconductor-semiconductor devices. In the latter case, accurate, nondestructive, and time-resolved parity measurements are a challenging issue. Here, we report on control and real-time parity measurement in a superconducting island embedded in a superconducting loop and realized in a hybrid two-dimensional heterostructure using a microwave resonator. To avoid microwave losses impeding time-resolved measurements, the device and readout resonator are located on separate chips, connected via flip-chip bonding, and couple inductively through vacuum. The superconducting resonator detects the parity-dependent circuit inductance, allowing for fast parity readout. We have resolved even- and odd-parity states with a signal-to-noise ratio of SNR ≈ 3 for an integration time of 20 μs and a detection fidelity exceeding 98%. The real-time parity measurement shows a state lifetime extending into the millisecond range. Our approach will lead to a better understanding of coherence-limiting mechanisms in superconducting quantum hardware and help to advance inductive-readout schemes for hybrid qubits.

DOI: 10.1103/PRXQuantum.5.030337

I. INTRODUCTION

The control and measurement of isolated quantum systems is a crucial task for the realization of practical quantum devices [1,2]. Quantum dots have recently emerged as an ideal platform for the realization of critical components for charge [3,4] and spin [5,6] qubits due to their ability to trap, control, and sense individual charge carriers using electrostatic means. Superconducting quantum dots possess an additional degree of freedom, given by the parity (even or odd) of unpaired excitations [7–12]. Performing real-time nondestructive charge parity readout is therefore a fundamental requirement in proposed topological quantum computing schemes [13–19] and Andreev spin qubits [20–22]. More generally, continuous monitoring of the parity of superconducting systems could shed new light on fast dynamics and on the fundamental mechanisms limiting coherence in superconducting hardware.

Hybrid superconductor-semiconductor systems such as InAs-Al combine electrostatic control, high mobility, and spin-orbit coupling, providing a promising pathway for the encoding of topologically protected quantum information [13,23]. For this purpose, investigating effects related to parity in hybrid systems is of critical importance and has recently motivated intense research [24–27]. Previous demonstrations have predominantly focused on measurements of parity-dependent switching supercurrents [12,24,28–31] detected with dc transport techniques. Such approaches are typically slow and require macroscopic leads for current injection, and measurements lead to destruction of the parity state. High-frequency parity- and charge-readout studies have revolved around reflectometry techniques, where the device under test has been embedded in an impedance-matching tank circuit [32,33] and addressed in the radio-frequency [34] or microwave domain [35–37], allowing the detection of charge transitions. Experiments studying parity effects in hybrid systems in the high-frequency domain have, so far, been almost exclusively performed in semiconductor nanowires. In this context, planar systems are emerging as a highly promising platform to realize devices

*Contact author: fni@zurich.ibm.com
†Present address: Institute of Physics, Czech Academy of Sciences, 162 00 Prague, Czech Republic

beyond nanowire-based approaches. Lithographic control over device geometry, combined with enhanced versatility and reproducibility, makes these systems ideal for advanced quantum architectures, including future topologically protected devices. However, time-resolved parity measurements in hybrid planar systems are challenging due to the requirement for high-quality readout circuitry and the need to mitigate dissipation in device substrates induced by high-energy particles, which can lead to the generation of nonequilibrium quasiparticles (QPs) [38–41]. Moreover, the challenging, and sometimes competing, fabrication requirements for integrating microwave hardware on planar hybrid systems [42–46] further increase the complexity and thus fast parity readout and QP dynamics studies remain to be demonstrated in planar systems.

In this paper, we present a novel approach to parity readout in a confined superconducting system. A planar superconducting island is embedded in a superconducting loop, which is inductively coupled to a high-Q-factor microwave resonator using a flip-chip approach. Parity in the superconducting island directly maps into the direction of the circulating supercurrent in the loop, allowing for fast and absolute parity readout. With respect to approaches based on measurements of switching currents [24,29], our readout technique does not require the system to be driven into the normal state. Furthermore, the inductive-readout approach offers significant advantages when the system charging energy is low, as it still allows parity-dependent supercurrent magnitude or direction detection. Compared to capacitive detection-based techniques, our method could also be less prone to sensitivity to environmental parasitic capacitances, resulting in improved performance and detection fidelity. In our system, the parity effect in the island is observed at zero magnetic field simultaneously with the presence of a low-energy bound state in the island. We demonstrate parity detection with a signal-to-noise ratio SNR ≈ 3 for an integration time of 20 μs with a detection fidelity for both parity states above 98%. By continuously monitoring the state of the island, parity-switching events are observed, enabling the estimation of a parity lifetime approaching millisecond time scales, with no measurable parity transitions within the parity-blockade regime. The combination of inductive-readout technology, the flip-chip approach, and the planar heterostructure will facilitate the coherent addressing and manipulation of hybrid quantum devices.

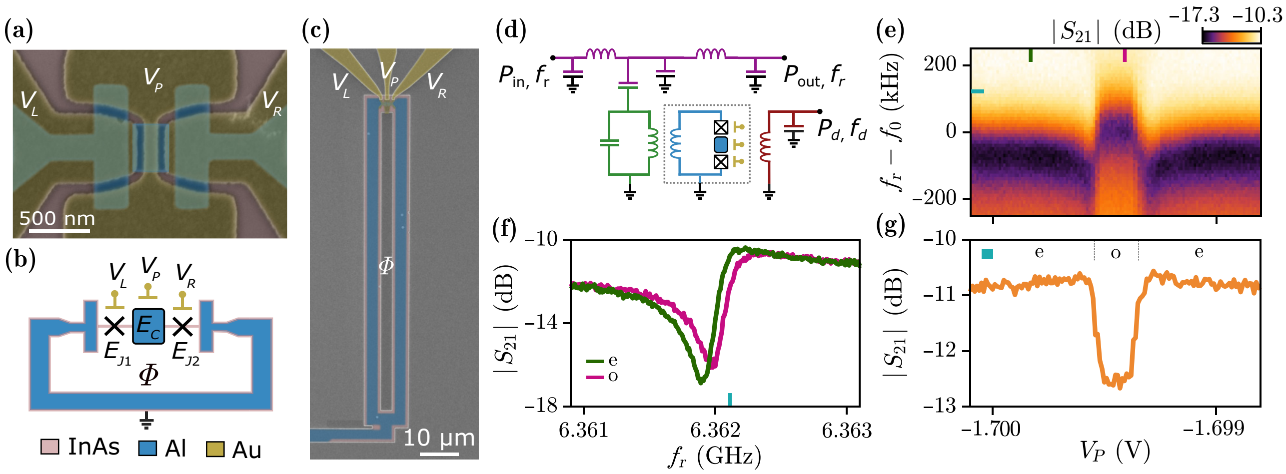

FIG. 1. The device and the parity-detection scheme. (a) A false-colored scanning electron micrograph of the superconducting island. The Al (blue) has been selectively removed to form a 250-nm-long and 400-nm-wide superconducting island coupled to wide superconducting T-shaped leads. The gate (yellow) with voltage V_P is used to suppress the parallel transport paths on both sides of the island and for tuning the charge occupation. Gates with voltages V_L and V_R (yellow) tune the coupling to the leads. (b) A schematic representation of the device under study, showing a superconducting island with charging energy E_C embedded in a superconducting loop tuned by the flux Φ. The coupling between the island and the leads is tuned via electrostatically controlled Josephson junctions with Josephson energies E_{J1} and E_{J2}. (c) A micrograph of the superconducting loop incorporating the gate-tunable island. (d) A schematic of the equivalent parity-detection circuit. The readout resonator (green) is inductively coupled to the superconducting loop (blue). The readout is performed by probing the complex transmission parameter $S_{21} = 10\log(P_{\text{out}}/P_{\text{in}})$ through a coplanar transmission line (purple) fabricated on the same chip as the resonator and capacitively coupled to the resonator. An additional drive line (red) present on the resonator chip enables two-tone microwave-spectroscopy measurements. (e) The magnitude of the transmission response $|S_{21}|$ in the Coulomb-blockade regime ($V_L = -1.755$ V and $V_R = -1.610$ V) as a function of the plunger voltage V_P and the offset readout frequency $f_r - f_0$, with $f_0 = 6.38198$ GHz. The shift of the resonator frequency indicates a transition between the two parity states. (f) Line cuts from the resonator response in (e) at positions indicated by the green and pink markers. An 80-kHz shift of the resonator frequency is present between even- (e) and odd- (o) parity states. (g) A line cut from (e) at the turquoise marker position as a function of V_P emphasizes the change in the resonator-magnitude response between even-and odd-parity states, demonstrating parity detection.

II. DEVICE AND READOUT SCHEME

In Fig. 1(a), we display a false-colored scanning electron micrograph of the active part of the device. The device consists of a floating superconducting island (blue) with dimensions of 250 nm × 400 nm that is coupled to the loop by two semiconducting junctions, each of length approximately 50 nm. The junctions are controlled with gate voltages V_L and V_R (yellow), realizing a tunable coupling to the superconducting leads (blue). The middle gate, energized by voltage V_P, is used both for the depletion of parallel transport paths around the island and for tuning the offset charge on the island. In Figs. 1(b) and 1(c), we show a schematic and a scanning electron micrograph of the full device, respectively. The relevant device parameters are the charging energy E_C of the island and the gate-controlled Josephson energies E_{J1} and E_{J2}, describing the energy required to add (remove) a single electron to (from) the island and the coupling between the island and the leads, respectively. To enable flux biasing, the island is embedded into a grounded superconducting loop (blue). The loop is patterned into the same InAs/Al heterostructure and is controlled via a magnetic flux Φ, generated by a home-made superconducting coil mounted on top of the printed circuit board that hosts the device.

The microwave measurements have relied on the flip-chip approach that has recently been pioneered in hybrid materials using nanowire-based [47] and planar devices [46]. The planar device and microwave components have been fabricated on separate chips to achieve high-quality devices and readout resonators ($Q_i = 35\,000$, $f_0 = 6.36198$ GHz). The chips have been connected with indium bump bonding. While the microwave resonators have been inductively coupled to the device via a vacuum gap ($d = 5$ µm) to sense the supercurrent in the device loop, galvanic connections between the two chips have been used to supply voltages to electrostatic gates and provide a grounding contact to the loop.

The simplified microwave measurement scheme is shown in Fig. 1(d). The transmission line (purple) is capacitively coupled to the readout resonator (green), which changes its frequency and loaded quality factor Q_L due to the current circulating in the loop (blue). The parity readout is performed by applying a probe signal P_{in} with frequency f_r to the left port of the transmission line and detecting the response P_{out} at the right output port at the same frequency f_r. For two-tone spectroscopy measurements, the additional drive line shown in Fig. 1(d) (red) is used to apply a continuous drive tone with power P_d and frequency f_d while monitoring the resonator transmission P_{out} at frequency f_r. More details about the fabrication and packaging are reported in Appendix A and the measurement setup is described in Appendix B. The data presented here have been collected on one device, whereas data from a second device are presented in the Supplemental Material [48].

III. PARITY EFFECT IN A SUPERCONDUCTING ISLAND

We first discuss the response of the resonator as a function of the gate voltage V_P when V_L and V_R are set sufficiently negative to result in a finite charging energy but still allow for a supercurrent to flow in the loop. Furthermore, the system is tuned to a regime with a strong parity effect. In Fig. 1(e), we display the magnitude of the transmission response $|S_{21}|$ as a function of V_P and the offset readout frequency $f_r - f_0$, with $f_0 = 6.38198$ GHz. As the gate voltage V_P is increased, a sharp change of the resonator frequency is observed in a narrow gate-voltage range around $V_P = -1.67$ V. In Fig. 1(f), we show line cuts of the resonator-magnitude response $|S_{21}|$ as a function of the readout frequency f_r at two V_P voltage values (dark green and pink markers) indicated in Fig. 1(e). At these values of V_P, both a shift of the resonator frequency by 80 kHz and an accompanying 12% change in its line width are visible. Remarkably, the frequency shift can be associated with a parity-dependent change in the direction of the circulating current, i.e., in the formation of a π junction for an odd-parity ground state. The circulating current results in a sign change of the effective inductance $L = [(2\pi/\Phi_0)\partial I_s(\varphi)/\partial\varphi]^{-1}$, producing a shift in the resonator frequency. Damping is associated with the formation of additional loss channels during the transition through a charge-degeneracy point, consistent with the variable-load-impedance model [49]. Monitoring the resonator response at fixed f_r [the turquoise marker position in Fig. 1(e)] as a function of V_P, as shown in Fig. 1(g), allows us to track the parity ground state of the superconducting island.

The energy diagram of a confined superconducting island in the absence of low-energy excitations is shown in Fig. 2(a). The energy of the island is characterized by periodic parabolas describing the even-parity states (blue) with charging energy E_C, the induced superconducting gap Δ (red), and a generic subgap state with energy δ (green), which in this case is above E_C. In this situation, the parity of the island remains even and sweeping gate voltages changes the charge occupation by two electrons at a time. Experimentally, this has been observed [see Fig. 2(b)] as a series of periodic features in the transmission-response magnitude $|S_{21}|$ as a function of V_P and V_R, measured at $\Phi = \Phi_0/2$. The regions in which the $|S_{21}|$ signal is enhanced are associated with crossing points of the electrostatic energy parabolas in Fig. 2(a). At these points, corresponding to resonant tunneling of Cooper pairs through the island, a sizeable supercurrent circulates in the loop, whereas between resonances the charge configuration is stable and the supercurrent is blocked. Therefore, $|S_{21}|$ monitored at a fixed f_r allows us to distinguish between the current flowing at charge-state degeneracy and its suppression in the blockade regime.

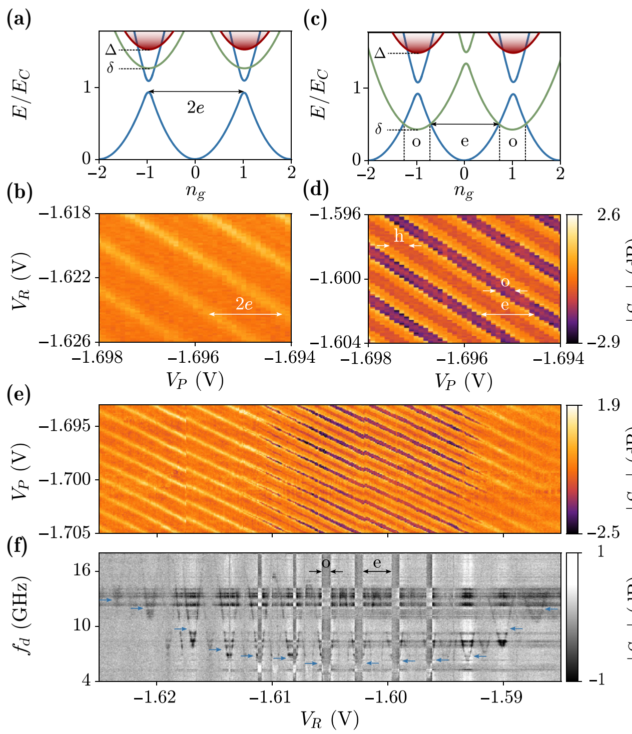

FIG. 2. The charge states of a superconducting island. (a) The electrostatic energy diagram of a Coulomb-blockaded superconducting island with charging energy E_C smaller than a subgap energy state δ (the 2e-periodic regime). (b) The experimentally measured transmission-response magnitude $|S_{21}|$ at $\Phi = \Phi_0/2$ as a function of the plunger gate voltage V_P and the right-barrier gate voltage V_R. The 2e-periodic Coulomb-blockade oscillations observed as a function of both voltages are consistent with the situation depicted in (a). (c) The same as (a) but for $E_C > \delta$, showing the parity effect with alternating even- and odd-parity valleys. (d) The same as (b) but in a gate regime in which the parity effect is present, leading to periodically alternating spacings for even- (e) and odd- (o) parity sectors. (e) An overview of the resonator-response magnitude $|S_{21}|$ at $\Phi = \Phi_0/2$ for broad ranges of V_P and V_R. Tuning of the parity effect is observed as a modulation of the periodicity between the Coulomb-blockade peaks as the voltage V_R is varied. (f) The two-tone spectroscopy measurement at $\Phi = \Phi_0/2$, showing the resonator-response magnitude $|S_{21}|$ as a function of the drive frequency f_d and the right-barrier voltage V_R in a gate regime in which the parity effect is present.

A significantly different situation is obtained when an excitation with energy $\delta < E_C$ is present in the spectrum [see Fig. 2(c)]. In this case, the crossing points between the lowest-energy parabolas (blue and green) become unevenly spaced and the superconducting island accepts single electrons. This has been measured in Fig. 2(d). The abrupt and periodic change in color of the $|S_{21}|$ response separates the two parity sectors. The odd-parity (o) state is associated with narrow and dark-color regions separated by larger bright and wider regions in which the parity is even (e). The additional features in the center of the even-parity sector (h), running parallel in gate space to the main parity transitions, are associated with transport processes involving excited states of the island. The crossings of the associated higher-energy parabolas [at a higher energy than shown in Fig. 2(c)] enable new transport channels and lead to a measurable effect on the current circulating in the loop visible in the even-parity valley [50].

In Fig. 2(e), we display $|S_{21}|$ at $\Phi = \Phi_0/2$ in a broader parameter space, where transitions between the two regimes discussed above are visible. The results in Fig. 2(e) strongly suggest that the charging energy of the superconducting island is generally smaller than the superconducting gap. However, a discrete Andreev state can occasionally be tuned to energies $\delta < E_C$, giving rise to parity transitions. In the case of Fig. 2(e), such a discrete state is predominantly controlled by V_R. In this particular case, the size of this parity-sensitive gate region is defined by the condition $\delta \approx E_C$, which is dependent on the gate lever arm and exact gate geometry. Incidentally, similar even-odd periodicity could be observed even in the absence of ABSs, when $\Delta < E_C$. In such a system, the parity effect will persist for wider ranges of the gate voltage. However, a large charging energy, together with a small superconducting gap, might lower the circulating supercurrent and reduce the microwave response of the circuit to parity changes.

More quantitative insights are gained by performing two-tone spectroscopy measurements, as shown in Fig. 2(f). We observe a driven transition (parabolas indicated by blue arrows), which is continuous and periodic as a function of V_R, with a periodicity consistent with 2e charging. We interpret the driven transition as excitations from the even-parity ground state to its excited state [blue curves in Figs. 2(a) and 2(c)] [51]. In a two-band model of a superconducting transistor [52], the minimum transition frequency is associated with the difference between the Josephson energies of the tunnel barriers coupling the island to the leads, $|E_{J2} - E_{J1}|$. At the edges of Fig. 2(f), the island is in the 2e regime and the parabolas have a minimum transition frequency of approximately 11 GHz, corresponding to a difference in the critical currents of right and left barriers of 4 nA. In the V_R range of Fig. 2(f), the right barrier likely transitions through a resonance that locally reduces $|E_{J2} - E_{J1}|$, lowering the minimum transition frequency (blue arrows). The resonance also increases the transmission through the island [44], tuning an ABS below the charging energy and giving rise to changes of ground-state parity, resulting in sharp color changes over finite regions of V_R [see the "e" and "o" labels in Fig. 2(f)]. From the transition frequency at which ground-state transitions first occur, a charging energy $E_C \approx 6.7$ GHz is estimated (see the Supplemental Material [48]).

We relate the faint parabolas appearing between 2e transitions [labeled with "h" in Fig. 2(d)] to higher-order transport processes. A QP from the gap edge relaxes and is temporarily trapped in the ABS energy level, before escaping to the leads [50]. This contributes to the resonator shift, similar to odd-parity occupation in the island. The visibility of such parabolas is expected to be suppressed by reducing the coupling to the leads, as well as reducing the QP density in the leads. Operating the device with less-transparent barriers could help mitigating such processes but would also require more sensitive readout architecture to detect smaller circulating supercurrents. The horizontal resonances in Fig. 2(d) are attributed to unintentional standing waves in the measurement circuit. Additional two-tone spectroscopy measurements are presented in the Supplemental Material [48].

IV. ESTIMATION OF SNR AND READOUT FIDELITY

Fast and continuous monitoring of the charge parity provides access to the fast dynamics of the system. The performance of our approach is quantified by the signal-to-noise ratio (SNR) and the measurement fidelity F. First, we have acquired the in-phase (I) and quadrature (Q) components of the resonator response at a fixed readout frequency $f_r =$ 6.36206 GHz and calculated the transmission-response magnitude $R = \sqrt{I^2 + Q^2}$ as a function of V_P for variable data-integration times τ_{int}. An exemplary R trace measured with $\tau_{\text{int}} = 50$ μs is depicted in Fig. 3(a), where two well-distinguishable levels of response are associated with even- and odd-parity states. The higher-order transport processes mentioned above are also visible as a dip in R centered at $V_P = -1.6955$ V. The I and Q map of Fig. 3(b) provides access to the amplitude and phase of the signal, which we use next to estimate the levels of the signal (S) and the noise (N). For this, we fit the resulting histogram to a two-dimensional (2D) bimodal Gaussian distribution. The signal level is defined as the distance between centers of the fitted Gaussians, whereas the noise is defined as the standard deviation of the Gaussians responsible for state broadening (for details, see Fig. 11).

To calculate the fidelity F of the parity-state assignment, we first project the histogram data along the axis connecting the centers of the two Gaussians to recover a one-dimensional (1D) histogram of the state distribution. Following this, the fidelities for the even and odd states are defined as $F_e = 1 - \int_{V_T}^{\infty} n_e(V)dV$ and $F_o = 1 - \int_{-\infty}^{V_T} n_o(V)dV$, respectively [34,53], where V_T is the threshold voltage, namely, the value of the output voltage that defines the separation between the assignment of data points to even- or odd-parity sectors, and n_e (n_o) is the probability density of the even (odd) state. The results for the fixed integration time $\tau_{\text{int}} = 50$ μs are shown in Fig. 3(c), where both state infidelities $1 - F_e$ (green) and $1 - F_o$ (pink) are plotted as a function of V_T. To define the

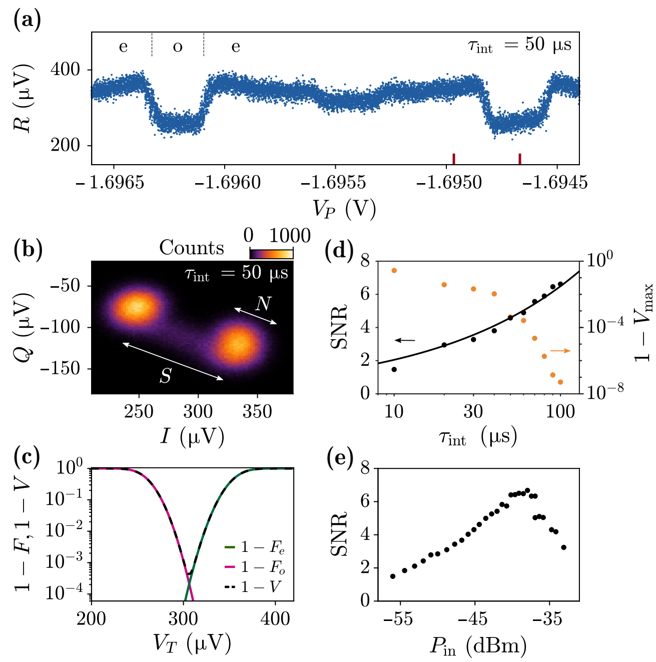

FIG. 3. The signal-to-noise ratio (SNR) and the detection fidelity. (a) The transmission-magnitude response R as a function of the plunger gate voltage V_P, measured at $V_L = -1.755$ V and $V_R = -1.609$ V, using a readout power $P_{\text{in}} = -44$ dBm (before attenuation) and an integration time $\tau_{\text{int}} = 50$ μs. Even- (e) and odd- (o) parity states are identified as different discrete levels in the response R. (b) The histogram of the resonator-magnitude response R decomposed into in-phase (I) and quadrature (Q) components encoding the two parity states. The signal (S) is characterized by the separation between the maxima of two centers, while the noise (N) is responsible for the broadening of the distribution. The data range used for the histogram is between the two red markers in (a). (c) The parity-readout infidelity for the even ($1 - F_e$, green) and odd ($1 - F_o$, pink) sectors, together with the readout invisibility $1 - V$ (black dashed) as a function of the threshold voltage V_T separating the two parity sectors for $\tau_{\text{int}} = 50$ μs. (d) The SNR together with a fit to an uncorrelated noise model (solid black line) and an extracted minimum invisibility $1 - V_{\text{max}}$ as a function of the integration time τ_{int}. (e) The dependence of the SNR on the readout power P_{in} (before attenuation) for $\tau_{\text{int}} = 50$ μs and $f_r = 6.36206$ GHz, showing a turnover behavior.

optimum value of V_T for the two parity states, the visibility is calculated as $V = F_e + F_o - 1$. Maximizing V allows us to find the optimal regime for F_e and F_o. In this case, the detection is optimized when $1 - V$ reaches a minimum at a threshold voltage $V_T = 306$ μV with a maximum obtained visibility $V_{\text{max}} = 0.9996$ (three nines) and a corresponding average measurement fidelity approaching 99.98%.

The extraction procedure for SNR and V_{max} is repeated for multiple τ_{int} values and summarized in Fig. 3(d). Both the SNR and V_{max} increase with increasing τ_{int}. The SNR trace in Fig. 3(d) has been fitted to an uncorrelated noise model [33], $\mathrm{SNR}(\tau_{\mathrm{int}}) = (S_{\tau_{\mathrm{int}}=1\ \mu\mathrm{s}}/N_{\tau_{\mathrm{int}}=1\ \mu\mathrm{s}})\sqrt{\tau_{\mathrm{int}}/(1\ \mu\mathrm{s})}$, where $S_{\tau_{\mathrm{int}}=1\ \mu\mathrm{s}} = 87\ \mu\mathrm{V}$ is the signal at $\tau_{\mathrm{int}} = 1\ \mu\mathrm{s}$ (used as a fit parameter) and $N_{\tau_{\mathrm{int}}=1\ \mu\mathrm{s}} = 135\ \mu\mathrm{V}$ is the noise at $\tau_{\mathrm{int}} = 1\ \mu\mathrm{s}$, determined by fitting $N(\tau_{\mathrm{int}}) \sim 1/\sqrt{\tau_{\mathrm{int}}}$. This has allowed the estimation of the integration time $\tau_{\mathrm{min}} = 2.4\ \mu\mathrm{s}$ for which SNR = 1 and the parity sensitivity $S = e\sqrt{\tau_{\mathrm{min}}} = 1.5 \times 10^{-3}\ e/\sqrt{\mathrm{Hz}}$. The average measurement fidelities at maximum visibility have been found to vary from 86% at $\tau_{\mathrm{int}} = 10\ \mu\mathrm{s}$ reaching 99.99999% (seven nines) at $\tau_{\mathrm{int}} = 100\ \mu\mathrm{s}$. The values obtained here for the SNR, the fidelity, and the visibility are comparable to those in previously reported charge- and parity-detection studies in hybrid materials [26,34].

Finally, in Fig. 3(e) we display the SNR dependence on the readout power P_{in} (before cryogenic attenuation) measured with $\tau_{\mathrm{int}} = 50\ \mu\mathrm{s}$ at a readout frequency $f_r = 6.36202$ GHz. The initial increase of P_{in} leads to a correlated increase in the SNR, reaching a maximum of SNR ≈ 6.7 at $P_{\mathrm{in}} = -38$ dBm. Beyond this optimal value, the SNR shows a strong downward trend. This turnover behavior is mainly caused by the signal S, while the noise N is only slightly affected in the P_{in} range under study. Here, the signal is set by the frequency shift and damping of the readout resonator, both of which decrease for larger P_{in} (see Fig. 10). For low powers, the decreased damping improves the signal, but past the threshold, the reduction in the frequency shift starts to dominate, which results in smaller signals. We additionally note that the SNR values presented here are likely affected by the $1/f$ noise due to the low sweep rate of the gate voltage V_P and therefore act as a lower bound for the SNR in time-resolved measurements. The SNR dependence on f_r is presented in Appendix C.

V. TIME-RESOLVED PARITY MONITORING

After assessing good parity sensitivity and detection fidelity, we now study the time-resolved dynamics in the planar island. To detect parity-transition events, the resonator-response magnitude R has been monitored for a time window of 900 ms with $\tau_{\mathrm{int}} = 30\ \mu\mathrm{s}$ for multiple values of V_L. The results are summarized in Fig. 4(a), where we show a subset of that time window spanning the first 250 ms. The full time traces are shown in the Supplemental Material [48]. Deep in the even-parity sector, where the charge configuration is fixed, the resonator-response level is stable in time [the purple trace in Fig. 4(b)]. In this case, the charging energy of the superconducting island energetically penalizes changes in the charge configuration, leading to a stable parity occupation. The steplike transitions in the blue and green traces in Fig. 4(b) are associated with parity-switching events following random-telegraph-noise behavior. Parity switching is solely observed close to charge degeneracy due to lifting of the protection by E_C there. Consequently, V_L tunes not only the preferred parity state but also the frequency of switching events. Additional measurements on gate-dependent parity switching are presented in the Supplemental Material [48], together with a discussion on gate stability.

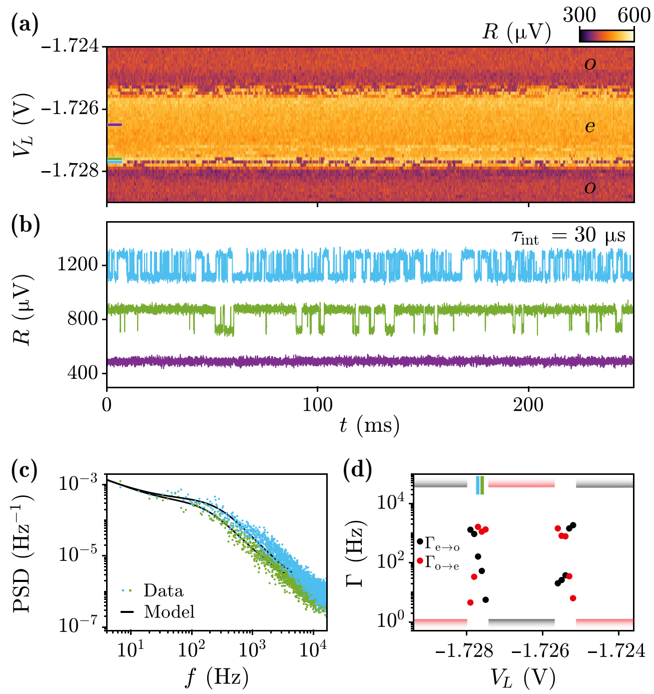

FIG. 4. Continuous parity monitoring. (a) The resonator-response magnitude R in the regime in which the parity effect is visible as a function of the measurement time t and the voltage V_L, for $\tau_{\mathrm{int}} = 30\ \mu\mathrm{s}$. Around the regions in which the parities are degenerate, the switching rates are enhanced compared to the rates away from degeneracy. (b) The time trace of the resonator response R close to parity degeneracy, showing parity-switching effects detected in real time (blue), a similar trace but further away from degeneracy, where the switching rate is reduced (green), and the time trace in the blockade regime, where the parity is fixed (purple). (c) The Welch power spectral density (PSD) as a function of the frequency f for the blue and green traces in (b), fitted to an asymmetric random-telegraph-noise model including a $1/f$ noise term. (d) The parity-switching rates $\Gamma_{e\to o}$ and $\Gamma_{o\to e}$ as a function of the voltage V_L in (a). The switching rate for the blue and green traces in (b) are indicated by blue and green markers, respectively. In the blockade regime, the lower and upper bounds on $\Gamma_{e\to o}$ and $\Gamma_{o\to e}$, shown as red and black lines, are limited by the length of the total recorded time trace (900 ms) and the integration time ($\tau_{\mathrm{int}} = 30\ \mu\mathrm{s}$).

The average transition rates in such a two-level system are quantified in the spectral domain using power-spectral-density (PSD) analysis [54,55]. For this, full 900-ms-long time traces have been converted to a Welch PSD [56], as shown in Fig. 4(c) for the green and blue time traces from Fig. 4(b). The PSD has then been fitted with an asymmetric random-telegraph-noise model including a $1/f$ noise term [57]. This has allowed us to infer the two parity-switching rates $\Gamma_{e\rightarrow o}$ and $\Gamma_{o\rightarrow e}$ associated with transitions between even-odd- and odd-even-parity sectors. For the green trace, we have obtained $\Gamma_{e\rightarrow o} = 53 \pm 1$ Hz and $\Gamma_{o\rightarrow e} = 1123 \pm 17$ Hz. For the blue trace, we have obtained $\Gamma_{e\rightarrow o} = 163 \pm 4$ Hz and $\Gamma_{o\rightarrow e} = 1624 \pm 24$ Hz, consistent with a smaller detuning. Asymmetric parity-switching rates are expected for devices with a large charging energy and reflect the preference for a specific ground-state parity. More information on parity-switching-rate extraction is presented in Appendix D.

The parity-switching-rate extraction procedure has been repeated at several V_L values from Fig. 4(a) and the results are summarized in Fig. 4(d). In the regions close to parity degeneracy, both rates develop a strong dependence on V_L and exchange their dominant behavior as a function of the detuning on both sides of the degeneracy. In the blockaded regime, the lowest detectable parity-switching rate is limited by the length of the total recorded time trace of 900 ms with $\min(\Gamma_{e\rightarrow o}) = \min(\Gamma_{o\rightarrow e}) = 1/(900\text{ ms})$, whereas the highest detectable rate is limited by the integration time $\tau_{\text{int}} = 30\ \mu\text{s}$, $\max(\Gamma_{e\rightarrow o}) = \max(\Gamma_{e\rightarrow o}) = 1/(30\ \mu\text{s})$. The two limits are schematically indicated as red and black regions in Fig. 4(d). The parity-switching rates $\Gamma_{e\rightarrow o}$ and $\Gamma_{o\rightarrow e}$ correspond to state lifetimes $T_e = 1/\Gamma_{e\rightarrow o}$ and $T_o = 1/\Gamma_{o\rightarrow e}$. For the time response shown in blue in Fig. 4(b), which has the most symmetric occupation of the two parity states, indicating close vicinity to charge degeneracy, we have found $T_e = 6.1 \pm 0.2$ ms and $T_o = 616 \pm 9\ \mu$s. Analysis of Fig. 4(d) indicates that $\Gamma_{e\rightarrow o} = \Gamma_{o\rightarrow e}$ for approximately 165 Hz, giving an estimated switching parity lifetime of 6 ms at charge degeneracy. This is, to our knowledge, the first reported estimate of the parity lifetime in a superconducting planar heterostructure.

Previous studies of InAs/Al nanowires [26,58] have shown a temperature-independent switching rate for temperatures below approximately 100 mK, followed by a steep increase in the switching rate, ascribed to thermal breaking of Cooper pairs. The low-temperature saturation could be ascribed to dielectric losses in the material platform, out-of-equilibrium phonons, or high-frequency photons. As our experiments have been performed at temperatures below 30 mK, we speculate that the contribution of thermal excitation on the reported switching rates is minimal. Further studies of switching rates as a function of temperature, magnetic field, and microwave-radiation parameters will guide toward a better understanding of the parity-switching mechanisms in hybrid systems. Improvements in the microwave setup might also allow to study the fast dynamics associated with excited states, which could only be detected via their time-averaged response [see the "h" label in Fig. 2(d) and the central dip in Fig. 3(a)]. Studying such states would require significant improvement of the SNR, making the central dip in Fig. 3(a) clearly visible for integration times significantly lower than 50 μs. This might be achieved by making sure that the drive and the readout signals do not lead to excess energy dissipation in the vicinity of the island, by improving the shielding of the device from external electromagnetic perturbations and by utilizing low-noise amplifiers at millikelvin temperatures.

VI. CONCLUSIONS

We have reported on a flip-chip-based inductive-detection scheme for the charge parity in a planar superconducting island. Our method combines the advantages of high-bandwidth readout technology with planar gate-tunable superconductor-semiconductor materials to achieve a high SNR for the ground-state readout of the parity. While the parity effect in our devices has been enabled by the low-energy excitation in the island, the readout technique is general and does not depend on the presence of such states. The combination of the flip-chip approach and inductive readout offers significant improvements whenever the experimental implementation involves circulating currents. Furthermore, it could facilitate the long-range coupling of different qubit subsystems, especially when large-scale devices using planar device technology become available. The long measured parity lifetimes constitute an important advantage in the context of hybrid qubits, where large numbers of gate operations can be performed before the parity information is lost. Additionally, the availability of parity-lifetime measurements will allow to constrain theoretical proposals for hybrid and protected qubit designs based on hybrid planar materials.

More generally, the inductive-readout approach is particularly beneficial in situations in which the devices subject to measurements are strongly coupled to superconducting leads, since inductive detection enables direct sensing of the parity-dependent supercurrent and does not rely on the presence of large or even finite charging energy. Typical examples include Andreev spin qubits and topological Majorana qubits. In contrast, in dissipative radio-frequency reflectometry or capacitive dispersive sensing techniques require sufficient charging energy in the system in order to impose fermionic parity, potentially introducing unwanted sources of noise or decoherence, and are very sensitive to parasitic capacitances in the environment. Interesting follow-up experiments include the study of superconducting-semiconducting hybrid qubits on a variety of material platforms and device geometries. The incorporation of spin-resolved Andreev levels into a planar quantum dot might suppress parity-switching processes due to the inherent charging energy of the system. We note that the presented inductive-detection technique would form a natural readout mechanism for such two-level systems, in which the supercurrent direction is directly mapped to a spin state. By integrating magnetic field-resilient microwave components, topological excitations at low energies could become accessible.

Coupling between quantum dots and topological modes will also enable parity-to-charge conversion, to which the readout methodology proposed here bears direct applicability. Finally, the geometry studied here can be extended to realize more advanced systems, including the recently proposed multiterminal [59] and multi-island devices [60].

Data presented in this work is available on Zenodo at Ref. [61].

ACKNOWLEDGMENTS

We thank the Cleanroom Operations Team of the Binnig and Rohrer Nanotechnology Center (BRNC) for their help and support. We are grateful to R. Žitko and L. Pavešić for helpful discussions. W.W. acknowledges support from the Swiss National Science Foundation (Grant No. 200020 207538). F.N. acknowledges support from the European Research Council (Grant No. 804273) and the Swiss National Science Foundation (Grant No. 200021 201082).

APPENDIX A: DEVICE FABRICATION

The superconducting islands were fabricated from an InAs/Al heterostructure grown on an InP substrate using electron-beam-lithography techniques. The semiconductor was etched in a solution of H_2O:$C_6H_8O_7$:H_3PO_4:H_2O_2 with composition 220:55:3:3. The epitaxial Al was etched with a short dip into 50°C Transene D to define the island and the superconducting loop. Under-bump metallization was evaporated on the device contacts [46] and the entire chip was covered by a dielectric layer consisting of 3-nm Al_2O_3 (110°C) and 15-nm HfO_2 (120°C), grown by thermal and plasma atomic layer deposition (ALD), respectively. The thermally grown Al_2O_3 served as a protective barrier for the plasma employed during the HfO_2 deposition, preventing degradation of the Al layer. Next, the fine features of the gate electrodes were deposited by electron evaporation of 5-nm Ti and 20-nm Au, followed by the evaporation of thicker gate features [Ti(5 nm)/Al(250 nm)/Ti(5 nm)/Au(100 nm)]. For both the inner and outer gates, lift-off was done in dimethyl sulfoxide (DMSO) at 120°C. A 45-nm layer of Al_2O_3 (120°C) was then deposited with plasma ALD. With wet etching in buffered hydrofluoric acid (BHF) at 7:1, RIE etching, and wet etching in the semiconductor etchant, the semiconductor stack was deep etched in the region between the devices and the bottom edge of the chip, to reduce resonator losses. Finally, the chip was diced into a 3 mm × 3 mm piece.

The readout resonators were fabricated on a high-resistivity Si wafer. First, 200 nm of Nb was sputtered over the entire chip, followed by deposition of a 57-nm AlO_2 hard mask by plasma ALD. The resonator features were defined by RIE in the hard mask. After resist removal in hot DMSO, inductively coupled plasma (ICP) etching with Cl_2 and Ar was used to pattern the Nb layer. Subsequently, the hard mask was removed with BHF 7:1. Next, the In bumps for flip-chip bonding were patterned by optical lithography and In evaporation. Finally, the wafer was diced into 6 mm × 9 mm chips. The resonator chip is identical to that shown in Fig. 1 of Ref. [46] and includes three $\lambda/4$ coplanar waveguide (CPW) resonators capacitively coupled to a common transmission line, drive lines, a ground plane, and dc control lines.

APPENDIX B: FLIP-CHIP TECHNIQUE AND MEASUREMENT SETUP

The connection between the device chip and the resonator chip was achieved through a flip-chip bonding process utilizing indium bump bonds and Karl Suss FC 150 flip-chip bonder. The indium bumps provided connections from bonding pads on the silicon (Si) chip to dc control lines used for gate electrodes and the grounding of the devices located on the indium phosphide (InP) chip. Several additional bump bonds were used to ensure the mechanical stability of the two-chip structure. The In bump bonds had a typical diameter of 50 μm and a height of 5 μm. Prior to bonding, the resonator chip underwent immersion in BHF at a ratio of 7:1 to eliminate the oxide layer from the indium bumps. The use of alignment markers, established during the fabrication of individual chips, helped to achieve precise alignment in the x-y direction and ensured a parallel orientation between the chips (below 1 μm accuracy). The final positions of the devices were adjusted to achieve the maximum coupling to the shorted ends of the $\lambda/4$ resonators but otherwise was optimized to avoid unintentional overlap with resonators. After alignment, the two chips were pressed together using thermocompression bonding. This resulted in a configuration in which the device chip faced downward on top of the resonator chip. The separation distance was regulated by adjusting the temperature and force applied during of flip-chip bonding process. The size of the flip-chip bonding pads was above 100 μm and each one contained several indium bumps for improved electrical connection and for mechanical stability.

The measurements have been performed in a BlueFors cryogen-free dilution refrigerator with a mixing-chamber base temperature of 9 mK. The wiring of the dilution refrigerator is illustrated in Fig. 5. The measurements depicted in Figs. 1 and 2 have been taken with a Keysight VNA B2911A vector network analyzer, while those in Figs. 3 and 4 were acquired with a Zurich Instruments SHFQA 8.5-GHz quantum analyzer. The readout tone with frequency f_r has been applied at port $P_{\rm in}$. For the two-tone spectroscopy measurements [see Fig. 2(f)], a continuous drive tone with frequency f_d has been applied at port $P_{\rm out}$ in Fig. 5. The drive signals have been attenuated by 66 dB and 39 dB, respectively, at different temperature stages of the dilution refrigerator. The signal transmitted through

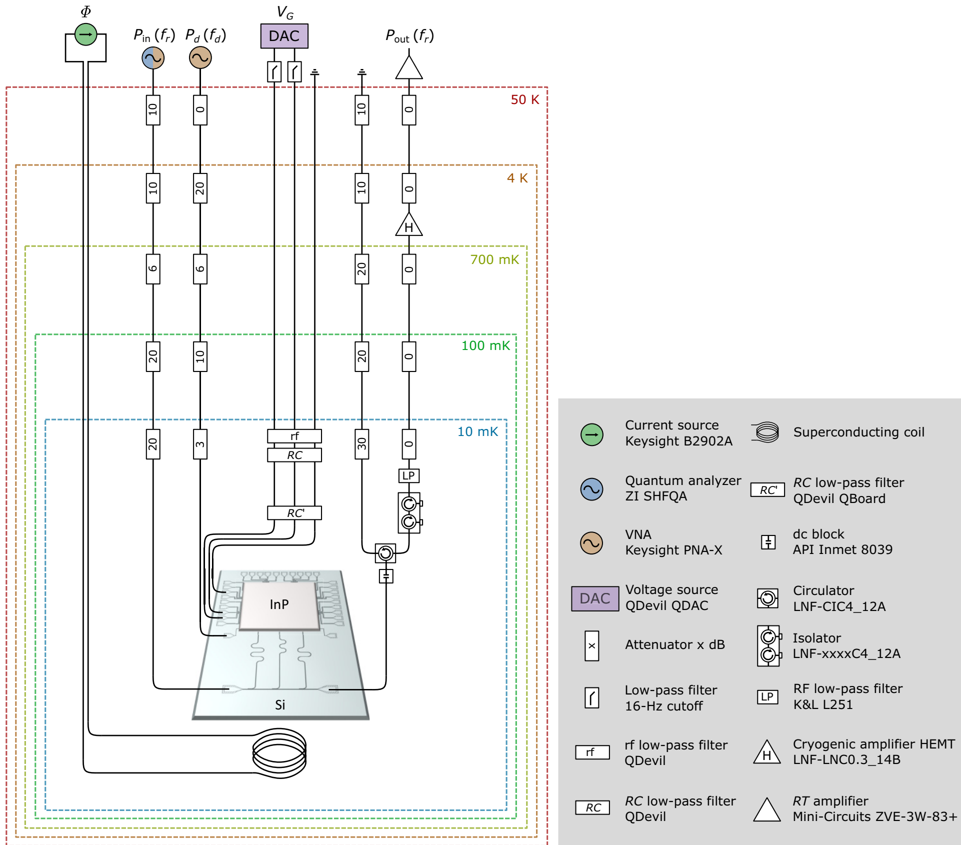

FIG. 5. The schematics of the measurement setup. The resonator readout and device drive tones with frequencies f_r and f_d were applied using a vector network analyzer (VNA) or quantum analyzer, corresponding to P_{in} and P_d, respectively. After 66-dB and 39-dB attenuation of P_{in} and P_d at different temperature stages of the dilution refrigerator, the signals reached the resonator chip. After the transmission, the readout signal passed through a dc block followed by a circulator, a dual isolator, and an rf low-pass filter. The signal was amplified with a cryogenic HEMT amplifier at 4 K and a room-temperature amplifier, before being detected (P_{out}) by the VNA or quantum analyzer. An extra rf line, which could be used for reflectometry measurements, stayed grounded during the experiments. The gates were controlled with digital-to-analog converter dc voltage sources. The dc lines were filtered using a home-made low-pass filter at room temperature, QDevil rf and *RC* filters at base temperature, and an *RC* filter on the printed circuit board. The applied dc signal reached the device via the resonator chip through the indium bumps. The external flux was applied by sourcing a direct current through a coil, mounted on top of the sample space. There was no additional shielding of the sample space because the refrigerator was equipped with a vector magnet, which was not utilized for the experiments.

the readout transmission line has passed through a dc block followed by a circulator, a dual isolator, and an rf low-pass filter. The signal has then been amplified with a cryogenic HEMT amplifier at 4 K and a room-temperature amplifier before being detected at the port labeled as P_{out}. The gates have been controlled with QDevil digital-to-analog converter dc voltage sources with 19-μV resolution. The dc lines have been filtered using a home-made low-pass filter at room temperature, QDevil rf and *RC* filters at base temperature, and an *RC* filter on the printed circuit board onto which the chip was mounted. The magnetic flux in the loop has been applied via a home-made superconducting coil mounted on top of the printed circuit board.

For each device, the superconducting island has been electrically defined by tuning the left and right island barrier gates with voltages V_L and V_R, respectively, as well as the plunger gate with voltage V_P. In Fig. 6(a), we show the flux dependence measured with all gate voltages grounded, resulting in a large circulating current. In Fig. 6(b), we show the flux dependence measured with all gates set to large negative voltages, resulting in suppression of the circulating current and the absence of a resonator response. The dependencies of $|S_{21}|$ on the various gate voltages and in different gate configurations are shown in Figs. 7(a)–7(e). The operating regime has been found first by setting $V_P = -1.5$ V and $\Phi = \Phi_0/2$ and by mapping $|S_{21}|$ as a function of V_L and V_R. A corner diagram as shown in Fig. 7(f) has been recorded, indicative of quantum dot formation. Here, fine tuning of each gate leads to the electrostatic regime presented in the main text. Additional electrostatic configurations, characterized by different coupling to the leads, are presented

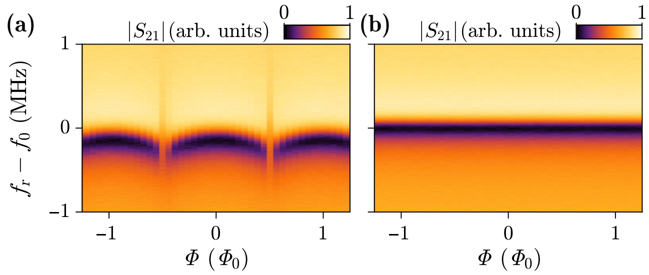

FIG. 6. The flux dependence in device 1. (a) The normalized resonator-magnitude response $|S_{21}|$ as a function of the flux Φ and the offset readout frequency $f_r - f_0$ at $V_G \equiv V_P = V_L = V_R = 0$. The distinct modulation of $|S_{21}|$ with respect to Φ reveals the coupling between the resonator and the device and indicates a large supercurrent in the device loop, carried by many Andreev bound states, located between the two superconducting leads [46]. (b) The same as (a) but at $V_G \equiv V_P = V_L = V_R = -1.8$ V. The depletion of the InAs quantum well between the leads suppresses the supercurrent.

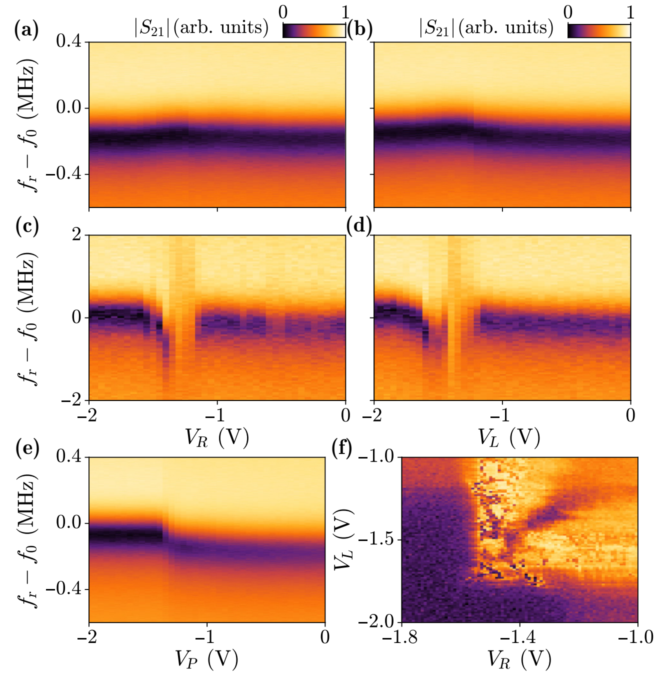

FIG. 7. The tune-up of device 1. (a) The normalized resonator-magnitude response $|S_{21}|$ as a function of the offset readout frequency $f_r - f_0$ and the barrier voltage V_R at $\Phi = \Phi_0/2$, $V_P = V_L = 0$. (b) The same as (a) but sweeping V_L and keeping $V_P = V_R = 0$. Transport channels parallel to the island limit the effect of the barrier gates V_R and V_L, respectively. (c) The same as (a) but at $V_P = -1.5$ V. (d) The same as (b) but at $V_P = -1.5$ V. Suppression of the parallel conductance channels increases the influence of the barrier gates on $|S_{21}|$. The coupling between the island and the lead decreases by reducing the density of Andreev bound states between them. This is observed for $V_R, V_L < -1$ V. Resonant transport around $V_L = -1.4$ V damps the resonator and causes a shift in its resonance frequency, both of which decrease for more negative barrier gate voltages. (e) The resonator-magnitude response $|S_{21}|$ as a function of the offset readout frequency $f_r - f_0$ and the plunger voltage V_P at $\Phi_0/2$, $V_L = V_R = 0$. (f) The resonator-magnitude response $|S_{21}|$ as a function of the barrier gate voltages V_L and V_R at $V_P = -1.5$ V and $f_r = 6.362$ GHz. The corner at $V_L \approx -1.7$ V and $V_R \approx -1.5$ V defines the gate range in which Coulomb blockade is observed.

in Figs. 8 and 9. Power-dependent measurements of Coulomb-blockade transitions and the resonator response are shown in Fig. 10.

The measurements in Figs. 2(b), 2(d), and 2(e) have been taken with resonator compensation. Each time, the slow-axis variable has been swept to the next value, $|S_{21}|$, as a function of the readout frequency f_r has been recorded, similar to Fig. 1(f), and the operating frequency has been offset by 90 kHz with respect to the frequency of the minimum. During postprocessing, the median of the resonator response along the fast axis has been subtracted from all data points, resulting in maps of the compensated resonator response as a function of the two gate voltages. The maps have been taken with $P_{\text{in}} = -44$ dBm, an integration time of 420 μs, and 15 averages.

APPENDIX C: READOUT CHARACTERIZATION

For the SNR calculation, the in-phase (I) and quadrature (Q) components of the readout resonator have been recorded as a function of the plunger gate voltage V_P with different integration times τ_{int} per data point, ranging from 10 to 100 μs. The readout frequency has been fixed at $f_r = 6.36206$ GHz and the power at $P_{\text{in}} = -44$ dBm. At each value of the plunger gate voltage, 5000 measurements of I and Q have been acquired (10 000 for $\tau_{\text{int}} = 10$ μs). Plotting the response magnitude $R = \sqrt{I^2 + Q^2}$ [see Fig. 3(a)] as a function of V_P reveals the two parity states, with the even state influenced by higher-order transport processes. In addition, the amount of recorded data as a function of V_P is much larger in the even-parity state than in the odd state. Therefore, we have selected a data set with 120 V_P values around a parity transition to have similar amount of data in the even- and odd-parity states. The I and Q values have then been plotted as a histogram with the bin size [Fig. 3(b)]. The histogram has been fitted with a sum of two 2D Gaussians,

$$A_1 e^{-(((b_{I1}-x)/c_{I1})^2+((b_{Q1}-y)/c_{Q1})^2)/2} + A_2 e^{-(((b_{I2}-x)/c_{I2})^2+((b_{Q2}-y)/c_{Q2})^2)/2}, \tag{C1}$$

where A_i is the height of the Gaussian, b_{Ii} (b_{Qi}) the center point, and c_{Ii} (c_{Qi}) is the width of the Gaussian on the I axis (Q axis), for $i = 1, 2$. The distance between the center points of the two Gaussians defines the strength of the signal S, whereas the quadratic sum of the average widths of the Gaussians, projected along S and perpendicular to

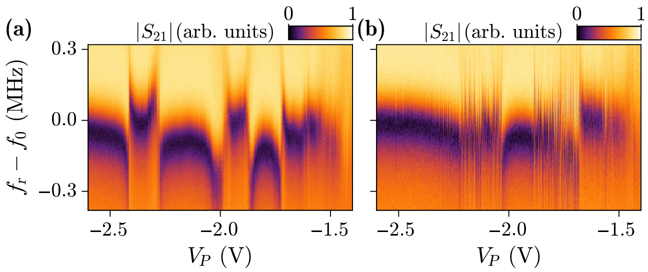

FIG. 8. The flux dependence in device 1 in different gate settings. (a) The normalized resonator-magnitude response $|S_{21}|$ as a function of the offset readout frequency $f_r - f_0$ and the plunger gate voltage V_P at $V_R = -1.47$ V, $V_L = -1.71$ V and $\Phi = \Phi_0/2$. The barrier gates put the system into a state in which there are isolated Andreev bound states (ABSs) but the island is still strongly coupled to the leads. The energy of these bound states is tuned by V_P, leading to anticrossings when the energy of the ABSs decreases below the resonator frequency consistent with a transmission close to one. (b) The same as (a) but at $V_L = -1.56$ V and $V_L = -1.72$ V. The weaker coupling of the island to the leads gives sharp transitions in the regime in which the ABS energies are below the resonator frequency. We assign these sharp lines to Coulomb transitions between even- and odd-parity states.

S using the polar form of ellipse equation, defines the noise N. The SNR is then defined as S/N and is given by

$$
\begin{aligned}
\mathrm{SNR} &= S/N, \\
S &= \sqrt{(b_{I1} - b_{I2})^2 + (b_{Q1} - b_{Q2})^2}, \\
N &= \sqrt{((|c_{\parallel S1}| + |c_{\perp S1}|)/2)^2 + ((|c_{\parallel S2}| + |c_{\perp S2}|)/2)^2},
\end{aligned}
\tag{C2}
$$

where $c_{\parallel Si}$ and $c_{\perp Si}$ are the widths of the Gaussian along and perpendicular to S for $i = 1, 2$. The SNR for all integration times is plotted in Fig. 3(d) and it has been fitted to $\mathrm{SNR}(\tau_{\mathrm{int}}) = (S_{\tau_{\mathrm{int}}=1\ \mu\mathrm{s}}/N_{\tau_{\mathrm{int}}=1\ \mu\mathrm{s}})\sqrt{\tau_{\mathrm{int}}/(1\ \mu\mathrm{s})}$, where $S_{\tau_{\mathrm{int}}=1\ \mu\mathrm{s}}$ represents the signal at $\tau_{\mathrm{int}} = 1\ \mu$s and has been used as a fit parameter and $N_{\tau_{\mathrm{int}}=1\ \mu\mathrm{s}} = 135\ \mu$V is the noise at $\tau_{\mathrm{int}} = 1\ \mu$s and determined by fitting $N(\tau_{\mathrm{int}}) \sim 1/\sqrt{\tau_{\mathrm{int}}}$, assuming S to be independent of τ_{int} [33].

The readout visibility is defined as $V = F_e + F_o - 1$, where F_e (F_o) is the fidelity of the even (odd) state, respectively. These fidelities are defined as $F_e = 1 - \int_{V_T}^{\infty} n_e(V)dV$ and $F_o = 1 - \int_{-\infty}^{V_T} n_o(V)dV$, where n_e (n_o) is the probability density of the even (odd) state [53]. The fidelity of a state describes the probability of an assignment of the resonator response to the correct parity sector, where V_T is the voltage threshold, describing the value of the transmission output voltage dividing the assignment to two parity sectors. The optimal assignment of V_T for detection is the value for which the visibility V is maximized. Maximizing V simultaneously also maximizes both detection fidelities, F_e and F_o. To calculate F_e, F_o, and V,

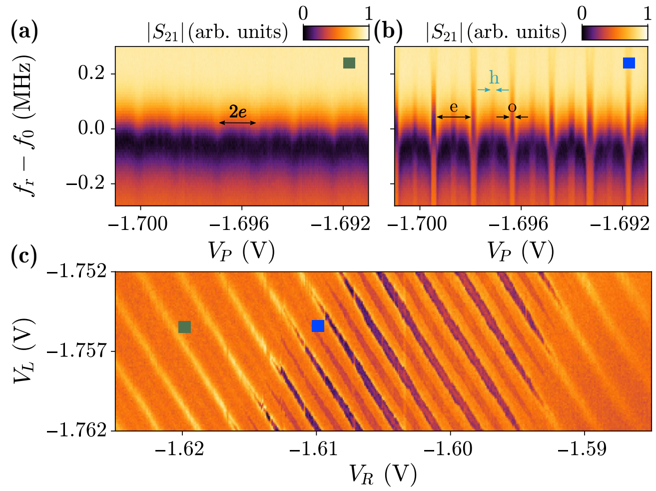

FIG. 9. Additional measurement data on device 1. (a) The normalized resonator-magnitude response $|S_{21}|$ as a function of the offset readout frequency $f_r - f_0$ and the plunger gate voltage V_P at $V_R = -1.610$ V, $V_L = -1.755$ V and $\Phi = \Phi_0/2$. The $2e$-periodic Coulomb-blockade oscillations are consistent with the charging energy of the island being lower than the bound-state energy ($E_C < \delta$). At Coulomb resonances, a shift in the resonator frequency is observed due to an enhanced circulating current in the device loop, which changes the inductance of the device. (b) The same as (a) but at $V_R = -1.620$ V. Here, $\delta < E_C$, which allows the number of quasiparticles on the superconducting island to be even or odd. The inductances of the even- (e) and odd- (o) parity states are different, resulting in distinct resonator responses. A slight modification of the even state is associated with higher-order transport processes (h) [50]. In the future, such quasiparticle poisoning from strong coupling to the leads could be suppressed with larger E_C. When the charging energy of the superconducting island is larger, a larger energy of the bound state is sufficient to enter the even-odd-parity regime, resulting in less coupling between the island and the leads. In that case, stronger coupling between resonator and device, resonators with higher Q factors, or an improvement in the readout setup is required to achieve the same readout performance. (c) The normalized resonator-magnitude response $|S_{21}|$ as a function of the barrier gate voltages V_L and V_R at $V_P = -1.7$ V. The gate-voltage map shows Coulomb-blockade oscillations because both barrier gates are able to tune the chemical potential of the superconducting island but with less efficiency compared to V_P. The bound-state energy δ is mainly modulated by V_R. If δ becomes lower than E_C, a transition from a $2e$-periodic to an even-odd regime happens. The odd-parity ground state emerges via splitting of the Coulomb resonance peak.

a line cut of the data in the I-Q plane [see Figs. 11(a) and 11(d)] has been taken along the signal S axis (100 points). The resulting 1D histogram as a function of the voltage $V_{\parallel}$ has been normalized by dividing the data by the sum of all counts [see Figs. 11(b) and 11(e)]. The normalized histogram has been fitted with two 1D Gaussians, given by

$$
A_1 e^{-((b_1 - x)/c_1)^2/2} + A_2 e^{-((b_2 - x)/c_2)^2/2}, \tag{C3}
$$

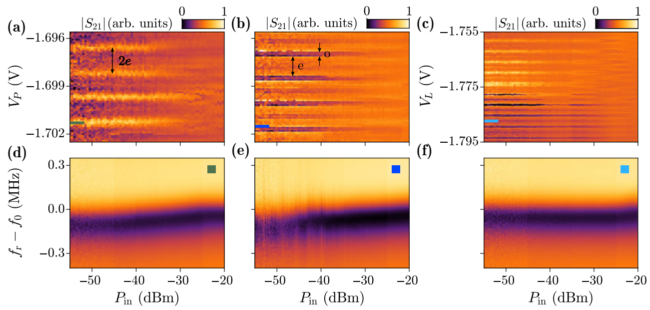

FIG. 10. The power-dependence measurements of device 1. (a) The normalized resonator-magnitude response $|S_{21}|$ as a function of the input readout power $P_{\rm in}$ and the plunger gate voltage V_P in the regime with $2e$-periodic Coulomb-blockade oscillations ($V_L = -1.760$ V, $V_R = -1.623$ V) at $\Phi = \Phi_0/2$. (b) The same as (a) but in the even-odd regime ($V_L = -1.795$ V, $V_R = -1.623$ V). (c) The normalized resonator-magnitude response $|S_{21}|$ as a function of the input readout power $P_{\rm in}$ and the barrier gate voltage V_L at $\Phi = \Phi_0/2$. (d) The normalized resonator-magnitude response $|S_{21}|$ as a function of the offset readout frequency $f_r - f_0$ and the input readout power $P_{\rm in}$ on a Coulomb resonance peak indicated by the green marker in (a). At low input powers, the resonator frequency is independent of $P_{\rm in}$ but the noise increases for decreasing $P_{\rm in}$. Above $P_{\rm in} = -44$ dBm, the resonator frequency shift decreases for increasing $P_{\rm in}$. (e) The same as (d) but on a transition between even- and odd-parity states indicated by the blue marker in (b). We observe a frequency shift and damping of the readout resonator as a function of $P_{\rm in}$. The damping increases significantly for $P_{\rm in} < -38$ dBm. (f) The same as (e) but in a Coulomb-blockade regime indicated by the turquoise marker in (c). Except for large input powers, the resonator frequency stays constant while the noise increases for decreasing $P_{\rm in}$.

where A_i is the height of the Gaussian, b_i the center point, and c_i is the width of the Gaussian for $i = 1, 2$. The integral in F_e (F_o) has been found through numerical integration of the corresponding 1D Gaussian with the composite trapezoidal rule using the PYTHON function NUMPY.TRAPZ. We have started (stopped) the integral by means of the threshold voltage V_T. Finally, the integral has been normalized because the histogram data has been normalized to the sum of both 1D Gaussians, resulting in

$$F_e = 1 - \int_{V_T}^{\infty} A_2 e^{-((b_2 - V_\parallel)/c_2)^2/2} dV_\parallel \Big/ \int_{-\infty}^{\infty} A_2 e^{-((b_2 - V_\parallel)/c_2)^2/2} dV_\parallel,$$

$$F_o = 1 - \int_{-\infty}^{V_T} A_1 e^{-((b_1 - V_\parallel)/c_1)^2/2} dV_\parallel \Big/ \int_{-\infty}^{\infty} A_1 e^{-((b_1 - V_\parallel)/c_1)^2/2} dV_\parallel. \quad \text{(C4)}$$

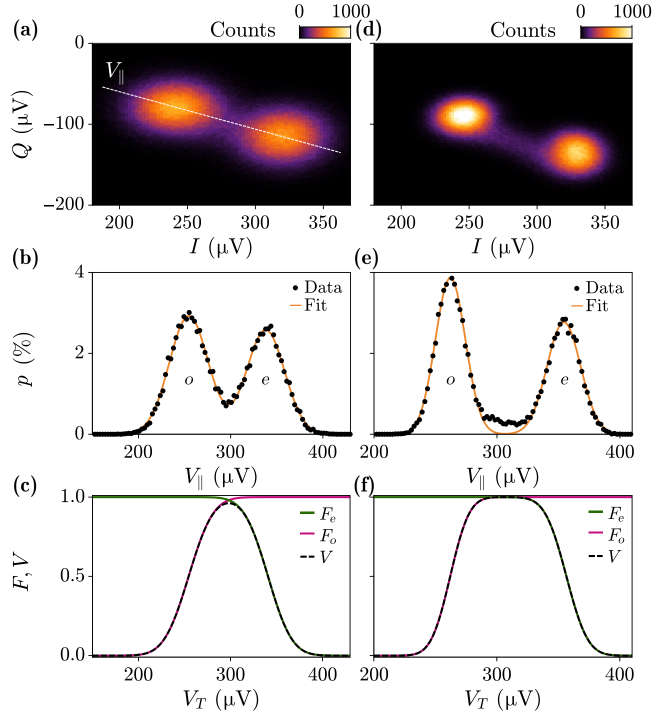

FIG. 11. The readout-fidelity determination. (a) The quadrature map of the two parity states for the integration time $\tau_{\rm int} = 20$ μs, plotted together with the line $V_\parallel$ along the signal axis. (b) A line cut from (a) along $V_\parallel$ normalized (black data points), plotted together with the fit to the sum of two Gaussians (orange). (c) The even- and odd-state fidelities F_e, F_o as well as the visibility V as a function of the threshold voltage V_T. The readout fidelity F_e (F_o) is calculated by numerical integration of the fit in (b), starting (stopping) at V_T. The readout visibility is calculated as $V = F_e + F_o - 1$. (d) The same as (a) but for $\tau_{\rm int} = 60$ μs. (e) The same as (b) but with the line cut along the signal axis from (d). The sum of two Gaussians cannot accurately fit the data due to a systematic error in the measurement. The slow sweep rate of the plunger gate voltage V_P during data acquisition results in a finite step width between even- and odd-parity states, as seen in Fig. 3. The finite step width can be mitigated by sweeping V_P faster; however, it does not affect the readout-fidelity calculation presented here. (f) The same as (c) using the fit curve from (e).

The fidelities and visibility as a function of V_T are plotted in Fig. 3(c) and Figs. 11(c) and 11(f). The readout-frequency dependence of the SNR is shown in Fig. 12.

APPENDIX D: PARITY-SWITCHING-RATE ESTIMATION

To estimate the parity-switching rate, we have acquired the time trace of the transmission-response magnitude R for different left-barrier gate voltages V_L, while the other gate voltages have been fixed at $V_R = -1.59800$ V and $V_P = -1.69219$ V. The readout frequency is $f_r = 6.36206$ GHz and the power is $P_{\rm in} = -40.5$ dBm. At each value of V_L, 30 001 data points have been recorded.

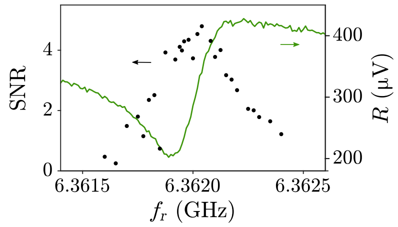

FIG. 12. The frequency-dependent SNR, as a function of the readout frequency f_r at a readout power $P_{\text{in}} = -44$ dBm, measured with an integration time $\tau_{\text{int}} = 50$ μs and plotted together with the resonator-response magnitude R in the even-parity state. The SNR dependence shows the pronounced maximum at a readout frequency $f_r = 6.36206$ GHz, which is due to the signal term (the noise term is independent of f_r). The signal term is determined by the change of the resonator-response magnitude between the even- and odd-parity states ($|R_e - R_o|$) resulting in the resonancelike shape, with a pronounced peak at f_r values, where the rate of change in R is strong.

The integration time has been set to 30 μs, resulting in a 900-ms-long time trace (neglecting the sampling rate of 0.5 ns). The data of the time trace at $V_L = -1.7277$ V [the blue time trace in Fig. 4(b)], which shows parity switching between the even- and odd-parity states due to random telegraph noise, has been converted into a histogram distributed into 20 bins along R. That histogram has been fitted with two 1D Gaussians as described in Eq. (C3). All time traces have been normalized based on these fit parameters, so that the transmission-response magnitude R have become 1 and 0 for the even- and odd-parity state, respectively.

Subsequently, the time traces have been used to calculate the Welch PSD. The calculation has been done using the PYTHON function SCIPY.SIGNAL.WELCH with sampling frequency $f_s = 1/(30\ \mu\text{s})$ and with segment length 5001. The resulting PSD has been fitted to an asymmetric random-telegraph-noise model including $1/f$ noise in the system using the following equation to estimate the transition rates from the even to odd $\Gamma_{e\to o}$ and from the odd to even $\Gamma_{o\to e}$ parity state [54,55]:

$$\text{PSD}(f) = \frac{8\Gamma_{e\to o}\Gamma_{o\to e}}{(\Gamma_{e\to o} + \Gamma_{o\to e})((\Gamma_{e\to o} + \Gamma_{o\to e})^2 + (2\pi f)^2)} + B/f + C, \tag{D1}$$

where B represents the influence of $1/f$ noise in the system and C is a constant describing the detection limit. The detection limit is given by the SNR and we start to approach it using 30-μs integration time, which can be seen by the flattening PSD curve at high frequencies. Therefore, C has been determined as the average of the PSD for the highest 100 frequency points. Since $1/f$ noise influences the slope of the PSD curve, the parameter B has been estimated empirically for every time trace with 2×10^{-6} times its PSD range. The transition rates $\Gamma_{e\to o}$ and $\Gamma_{o\to e}$ have been used as free fit parameters. Since Eq. (D1) is symmetric with respect to $\Gamma_{e\to o}$ and $\Gamma_{o\to e}$, the initial guess determines which of the two quantities is larger.

The maximum and minimum detectable transition rates have been set by the total time of the time trace and the integration time, respectively. Therefore, the lower bound of the rates is 1/(900 ms) (total measurement time) and the upper bound is 1/(30 μs) (integration time). For resonator-response levels that are stable within the measured time, such as the purple time trace in Fig. 4(b), its $\Gamma_{e\to o}$ and $\Gamma_{o\to e}$ have been assigned to the boundary rates.

[1] A. Blais, A. L. Grimsmo, S. M. Girvin, and A. Wallraff, Circuit quantum electrodynamics, Rev. Mod. Phys. **93**, 025005 (2021).

[2] Y. Y. Gao, M. A. Rol, S. Touzard, and C. Wang, Practical guide for building superconducting quantum devices, PRX Quantum **2**, 040202 (2021).

[3] D. Kim, D. Ward, C. Simmons, J. K. Gamble, R. Blume-Kohout, E. Nielsen, D. Savage, M. Lagally, M. Friesen, S. Coppersmith, *et al.*, Microwave-driven coherent operation of a semiconductor quantum dot charge qubit, Nat. Nanotechnol. **10**, 243 (2015).

[4] K. Petersson, J. Petta, H. Lu, and A. Gossard, Quantum coherence in a one-electron semiconductor charge qubit, Phys. Rev. Lett. **105**, 246804 (2010).

[5] A. J. Weinstein, M. D. Reed, A. M. Jones, R. W. Andrews, D. Barnes, J. Z. Blumoff, L. E. Euliss, K. Eng, B. H. Fong, S. D. Ha, *et al.*, Universal logic with encoded spin qubits in silicon, Nature **615**, 817 (2023).

[6] S. G. Philips, M. T. Madzik, S. V. Amitonov, S. L. de Snoo, M. Russ, N. Kalhor, C. Volk, W. I. Lawrie, D. Brousse, L. Tryputen, *et al.*, Universal control of a six-qubit quantum processor in silicon, Nature **609**, 919 (2022).

[7] M. Tuominen, J. Hergenrother, T. Tighe, and M. Tinkham, Experimental evidence for parity-based 2e periodicity in a superconducting single-electron tunneling transistor, Phys. Rev. Lett. **69**, 1997 (1992).

[8] J. Aumentado, M. W. Keller, J. M. Martinis, and M. H. Devoret, Nonequilibrium quasiparticles and 2e periodicity in single-Cooper-pair transistors, Phys. Rev. Lett. **92**, 066802 (2004).

[9] J. G. Lu, J. M. Hergenrother, and M. Tinkham, Parity effect in superconducting islands with increasing lengths, Phys. Rev. B **57**, 120 (1998).

[10] O. Naaman and J. Aumentado, Time-domain measurements of quasiparticle tunneling rates in a single-Cooper-pair transistor, Phys. Rev. B **73**, 172504 (2006).

[11] A. J. Ferguson, N. A. Court, F. E. Hudson, and R. G. Clark, Microsecond resolution of quasiparticle tunneling in the single-Cooper-pair transistor, Phys. Rev. Lett. **97**, 106603 (2006).

[12] J. A. Van Dam, Y. V. Nazarov, E. P. Bakkers, S. De Franceschi, and L. P. Kouwenhoven, Supercurrent reversal in quantum dots, Nature **442**, 667 (2006).

[13] D. Aasen, M. Hell, R. V. Mishmash, A. Higginbotham, J. Danon, M. Leijnse, T. S. Jespersen, J. A. Folk, C. M. Marcus, K. Flensberg, *et al.*, Milestones toward Majorana-based quantum computing, Phys. Rev. X **6**, 031016 (2016).

[14] K. Gharavi, D. Hoving, and J. Baugh, Readout of Majorana parity states using a quantum dot, Phys. Rev. B **94**, 155417 (2016).

[15] L. Dai, W. Kuo, and M.-C. Chung, Extracting entangled qubits from Majorana fermions in quantum dot chains through the measurement of parity, Sci. Rep. **5**, 11188 (2015).

[16] T. Karzig, C. Knapp, R. M. Lutchyn, P. Bonderson, M. B. Hastings, C. Nayak, J. Alicea, K. Flensberg, S. Plugge, Y. Oreg, *et al.*, Scalable designs for quasiparticle-poisoning-protected topological quantum computation with Majorana zero modes, Phys. Rev. B **95**, 235305 (2017).

[17] S. Plugge, A. Rasmussen, R. Egger, and K. Flensberg, Majorana box qubits, New J. Phys **19**, 012001 (2017).

[18] G. Szechenyi and A. Palyi, Parity-to-charge conversion for readout of topological Majorana qubits, Phys. Rev. B **101**, 235441 (2020).

[19] J. Schulenborg, S. Krojer, M. Burrello, M. Leijnse, and K. Flensberg, Detecting Majorana modes by readout of poisoning-induced parity flips, Phys. Rev. B **107**, 121401 (2023).

[20] L. Tosi, C. Metzger, M. F. Goffman, C. Urbina, H. Pothier, S. Park, A. L. Yeyati, J. Nygård, and P. Krogstrup, Spin-orbit splitting of Andreev states revealed by microwave spectroscopy, Phys. Rev. X **9**, 011010 (2019).

[21] M. Hays, V. Fatemi, D. Bouman, J. Cerrillo, S. Diamond, K. Serniak, T. Connolly, P. Krogstrup, J. Nygaard, A. Levy Yeyati, *et al.*, Coherent manipulation of an Andreev spin qubit, Science **373**, 430 (2021).

[22] M. Pita-Vidal, A. Bargerbos, R. Zitko, L. J. Splitthoff, L. Grunhaupt, J. J. Wesdorp, Y. Liu, L. P. Kouwenhoven, R. Aguado, B. van Heck, *et al.*, Direct manipulation of a superconducting spin qubit strongly coupled to a transmon qubit, Nat. Phys. **19**, 1110 (2023).

[23] M. Leijnse and K. Flensberg, Parity qubits and poor man's Majorana bound states in double quantum dots, Phys. Rev. B **86**, 134528 (2012).

[24] J.-Y. Wang, C. Schrade, V. Levajac, D. van Driel, K. Li, S. Gazibegovic, G. Badawy, R. L. Op het Veld, J. S. Lee, M. Pendharkar, *et al.*, Supercurrent parity meter in a nanowire Cooper pair transistor, Sci. Adv. **8**, 9896 (2022).

[25] E. T. Mannila, V. F. Maisi, H. Q. Nguyen, C. M. Marcus, and J. P. Pekola, Detecting parity effect in a superconducting device in the presence of parity switches, Phys. Rev. B **100**, 020502 (2019).

[26] H. Nguyen, D. Sabonis, D. Razmadze, E. Mannila, V. Maisi, D. van Zanten, E. O'Farrell, P. Krogstrup, F. Kuemmeth, J. Pekola, *et al.*, Electrostatic control of quasiparticle poisoning in a hybrid semiconductor-superconductor island, Phys. Rev. B **108**, L041302 (2023).

[27] A. P. Higginbotham, S. M. Albrecht, G. Kiršanskas, W. Chang, F. Kuemmeth, P. Krogstrup, T. S. Jespersen, J. Nygård, K. Flensberg, and C. M. Marcus, Parity lifetime of bound states in a proximitized semiconductor nanowire, Nat. Phys. **11**, 1017 (2015).

[28] T. M. Eiles, J. M. Martinis, and M. H. Devoret, Even-odd asymmetry of a superconductor revealed by the Coulomb blockade of Andreev reflection, Phys. Rev. Lett. **70**, 1862 (1993).

[29] D. J. Van Woerkom, A. Geresdi, and L. P. Kouwenhoven, One minute parity lifetime of a NbTiN Cooper-pair transistor, Nat. Phys. **11**, 547 (2015).

[30] D. Szombati, S. Nadj-Perge, D. Car, S. Plissard, E. Bakkers, and L. Kouwenhoven, Josephson ϕ_0-junction in nanowire quantum dots, Nat. Phys. **12**, 568 (2016).

[31] D. Razmadze, E. O'Farrell, P. Krogstrup, and C. Marcus, Quantum dot parity effects in trivial and topological Josephson junctions, Phys. Rev. Lett. **125**, 116803 (2020).

[32] R. Schoelkopf, P. Wahlgren, A. Kozhevnikov, P. Delsing, and D. Prober, The radio-frequency single-electron transistor (rf-set): A fast and ultrasensitive electrometer, Science **280**, 1238 (1998).

[33] C. Barthel, M. Kjærgaard, J. Medford, M. Stopa, C. M. Marcus, M. Hanson, and A. C. Gossard, Fast sensing of double-dot charge arrangement and spin state with a radio-frequency sensor quantum dot, Phys. Rev. B **81**, 161308 (2010).

[34] D. Razmadze, D. Sabonis, F. K. Malinowski, G. C. Ménard, S. Pauka, H. Nguyen, D. M. van Zanten, C. Eoin, J. Suter, P. Krogstrup, *et al.*, Radio-frequency methods for Majorana-based quantum devices: Fast charge sensing and phase-diagram mapping, Phys. Rev. Appl. **11**, 064011 (2019).

[35] M.-C. Harabula, T. Hasler, G. Fülöp, M. Jung, V. Ranjan, and C. Schönenberger, Measuring a quantum dot with an impedance-matching on-chip superconducting *LC* resonator at gigahertz frequencies, Phys. Rev. Appl. **8**, 054006 (2017).

[36] D. de Jong, J. van Veen, L. Binci, A. Singh, P. Krogstrup, L. P. Kouwenhoven, W. Pfaff, and J. D. Watson, Rapid detection of coherent tunneling in an InAs nanowire quantum dot through dispersive gate sensing, Phys. Rev. Appl. **11**, 044061 (2019).

[37] D. de Jong, C. G. Prosko, D. M. Waardenburg, L. Han, F. K. Malinowski, P. Krogstrup, L. P. Kouwenhoven, J. V. Koski, and W. Pfaff, Rapid microwave-only characterization and readout of quantum dots using multiplexed gigahertz-frequency resonators, Phys. Rev. Appl. **16**, 014007 (2021).

[38] K. Karatsu, A. Endo, J. Bueno, P. De Visser, R. Barends, D. Thoen, V. Murugesan, N. Tomita, and J. Baselmans, Mitigation of cosmic ray effect on microwave kinetic inductance detector arrays, Appl. Phys. Lett. **114**, 032601 (2019).

[39] X. Pan, Y. Zhou, H. Yuan, L. Nie, W. Wei, L. Zhang, J. Li, S. Liu, Z. H. Jiang, G. Catelani, *et al.*, Engineering superconducting qubits to reduce quasiparticles and charge noise, Nat. Commun. **13**, 7196 (2022).

[40] C. D. Wilen, S. Abdullah, N. Kurinsky, C. Stanford, L. Cardani, G. d'Imperio, C. Tomei, L. Faoro, L. Ioffe, C. Liu, *et al.*, Correlated charge noise and relaxation errors in superconducting qubits, Nature **594**, 369 (2021).

[41] M. McEwen, L. Faoro, K. Arya, A. Dunsworth, T. Huang, S. Kim, B. Burkett, A. Fowler, F. Arute, J. C. Bardin, *et al.*, Resolving catastrophic error bursts from cosmic rays in large arrays of superconducting qubits, Nat. Phys. **18**, 107 (2022).

[42] L. Casparis, M. R. Connolly, M. Kjaergaard, N. J. Pearson, A. Kringhøj, T. W. Larsen, F. Kuemmeth, T. Wang, C. Thomas, S. Gronin, *et al.*, Superconducting gatemon qubit based on a proximitized two-dimensional electron gas, Nat. Nanotechnol. **13**, 915 (2018).
[43] C. Baumgartner, L. Fuchs, L. Frész, S. Reinhardt, S. Gronin, G. C. Gardner, M. J. Manfra, N. Paradiso, and C. Strunk, Josephson inductance as a probe for highly ballistic semiconductor-superconductor weak links, Phys. Rev. Lett. **126**, 037001 (2021).
[44] V. Chidambaram, A. Kringhøj, L. Casparis, F. Kuemmeth, T. Wang, C. Thomas, S. Gronin, G. C. Gardner, Z. Cui, C. Liu, *et al.*, Microwave sensing of Andreev bound states in a gate-defined superconducting quantum point contact, Phys. Rev. Res. **4**, 023170 (2022).
[45] B. Harlech-Jones, S. Waddy, J. Witt, D. Govender, L. Casparis, E. Martinez, R. Kallaher, S. Gronin, G. Gardner, M. Manfra, *et al.*, Local and non-local microwave impedance of a three-terminal hybrid device, arXiv:2207.12516.
[46] M. Hinderling, D. Sabonis, S. Paredes, D. Haxell, M. Coraiola, S. ten Kate, E. Cheah, F. Krizek, R. Schott, W. Wegscheider, *et al.*, Flip-chip-based microwave spectroscopy of Andreev bound states in a planar Josephson junction, Phys. Rev. App. **19**, 054026 (2023).
[47] P. Zellekens, R. S. Deacon, P. Perla, D. Grützmacher, M. I. Lepsa, T. Schäpers, and K. Ishibashi, Microwave spectroscopy of Andreev states in InAs nanowire-based hybrid junctions using a flip-chip layout, Commun. Phys. **5**, 267 (2022).
[48] See the Supplemental Material at http://link.aps.org/supplemental/10.1103/PRXQuantum.5.030337 for the additional single- and two-tone measurements from a first and a second device, coupling-factor estimation, and details of the time-resolved measurements, which includes Refs. [62–64].
[49] R. Haller, G. Fülöp, D. Indolese, J. Ridderbos, R. Kraft, L. Y. Cheung, J. H. Ungerer, K. Watanabe, T. Taniguchi, D. Beckmann, R. Danneau, P. Virtanen, and C. Schönenberger, Phase-dependent microwave response of a graphene Josephson junction, Phys. Rev. Res. **4**, 013198 (2022).
[50] S. M. Albrecht, E. B. Hansen, A. P. Higginbotham, F. Kuemmeth, T. S. Jespersen, J. Nygård, P. Krogstrup, J. Danon, K. Flensberg, and C. M. Marcus, Transport signatures of quasiparticle poisoning in a Majorana island, Phys. Rev. Lett. **118**, 137701 (2017).
[51] A. Proutski, D. Laroche, B. van'T Hooft, P. Krogstrup, J. Nygård, L. P. Kouwenhoven, and A. Geresdi, Broadband microwave spectroscopy of semiconductor nanowire-based Cooper-pair transistors, Phys. Rev. B **99**, 220504 (2019).
[52] P. Joyez, Ph.D. thesis, Université Pierre et Marie Curie-Paris VI (1995).
[53] C. Barthel, D. J. Reilly, C. M. Marcus, M. P. Hanson, and A. C. Gossard, Rapid single-shot measurement of a singlet-triplet qubit, Phys. Rev. Lett. **103**, 160503 (2009).
[54] D. Ristè, C. Bultink, M. J. Tiggelman, R. N. Schouten, K. W. Lehnert, and L. DiCarlo, Millisecond charge-parity fluctuations and induced decoherence in a superconducting transmon qubit, Nat. Commun. **4**, 1913 (2013).
[55] F. Luthi, T. Stavenga, O. W. Enzing, A. Bruno, C. Dickel, N. K. Langford, M. A. Rol, T. S. Jespersen, J. Nygård, P. Krogstrup, and L. DiCarlo, Evolution of nanowire transmon qubits and their coherence in a magnetic field, Phys. Rev. Lett. **120**, 100502 (2018).
[56] P. Welch, The use of fast Fourier transform for the estimation of power spectra: A method based on time averaging over short, modified periodograms, IEEE Trans. Audio Electroacoust. **15**, 70 (1967).
[57] B. G. Christensen, C. D. Wilen, A. Opremcak, J. Nelson, F. Schlenker, C. H. Zimonick, L. Faoro, L. B. Ioffe, Y. J. Rosen, J. L. DuBois, B. L. T. Plourde, and R. McDermott, Anomalous charge noise in superconducting qubits, Phys. Rev. B **100**, 140503 (2019).
[58] O. Erlandsson, D. Sabonis, A. Kringhøj, T. W. Larsen, P. Krogstrup, K. D. Petersson, and C. M. Marcus, Parity switching in a full-shell superconductor-semiconductor nanowire qubit, Phys. Rev. B **108**, L121406 (2023).
[59] F. J. Matute-Cañadas, L. Tosi, and A. L. Yeyati, Quantum circuits with multiterminal Josephson-Andreev junctions, PRX Quantum **5**, 020340 (2024).
[60] D. M. Pino, R. S. Souto, and R. Aguado, Minimal Kitaev-transmon qubit based on double quantum dots, Phys. Rev. B **109**, 075101 (2024).
[61] https://doi.org/10.5281/zenodo.12781753.
[62] C. W. J. Beenakker, Universal limit of critical-current fluctuations in mesoscopic Josephson junctions, Phys. Rev. Lett. **67**, 3836 (1991).
[63] P. F. Bagwell, Suppression of the Josephson current through a narrow, mesoscopic, semiconductor channel by a single impurity, Phys. Rev. B **46**, 12573 (1992).
[64] C. Janvier, L. Tosi, L. Bretheau, Ç. Ö. Girit, M. Stern, P. Bertet, P. Joyez, D. Vion, D. Esteve, M. F. Goffman, H. Pothier, and C. Urbina, Coherent manipulation of Andreev states in superconducting atomic contacts, Science **349**, 1199 (2015).